An Improved High Linearity Active CMOS Mixer: Design and Volterra Series Analysis

Marzieh Mollaalipour and Hossein Miar-Naimi, *Member, IEEE*

***Abstract*—The linearity and noise requirements in multistandard applications make the design of mixers so challenging. In this paper a new highly linear CMOS mixer is proposed that utilizes second- and third-order distortion cancellation mechanisms using second harmonic injection technique, also an in-depth analysis of the mixer is presented too. The proposed circuit can work for wide channel bandwidth applications. Full Volterra series analysis of the transconductance stage of the proposed mixer is reported to show the effectiveness of the IM_2 injection technique. The analysis of the mechanisms responsible for generating the fundamental tone, the second- and the third-order intermodulation distortions in the switching stage along with an LC filter is also reported. Simulations using TSMC 0.18 μm CMOS model technology demonstrate that IIP3 and IIP2 of the proposed mixer have 10 dB and 26 dB improvements in comparison with the conventional Gilbert-type mixer while the NF doesn't change significantly. The mixer achieves a conversion gain of 15 dB from a 1.8 V supply. The additional circuits used for the IM2 and IM3 cancellation mechanisms have a total current consumption of less than 1 mA.**

***Index Terms*—Gilbert-cell mixers, high linearity, second- and third-order input intercept point (IIP2 and IIP3), second- and third-order intermodulations ($\mathrm{IM}_2, \mathrm{IM}_3$).**

I. Introduction

DIRECT conversion receivers (DCR) are attractive because of the possibility for high integration level, low cost, and simplicity of baseband circuitry as compared with other type of receivers.

Unfortunately this kind of receiver suffers from high second- and third-order intermodulations ($\mathrm{IM}_2, \mathrm{IM}_3$). Among different sections of a receiver like LNA and mixer, the down-conversion mixer is the dominant source of IM_2 and IM_3 in a direct conversion receiver [1], [2]. The IM_2 and IM_3 generated by LNA are filtered out by its output narrowband LC resonator and ac-coupling between LNA and mixer.

In the DCR, the double-balanced Gilbert mixer has been widely used as the down converter in wireless receivers due to its low RF and local oscillator (LO) feed-through [3], [4].

Different linearization techniques have been proposed for the RF mixer applications in CMOS processes.

The even-order nonlinearities can be reduced by using differential topology and symmetric layout, but the required performance especially for cellular phone applications cannot be met [5]. However, in practice, the presence of mismatches in the load and the switching transistors result in even-order intermodulations in the signal path; therefore, using second-order input intercept point (IIP2) improvement techniques are necessary.

An effective but expensive solution to improve IIP2 is to use an external surface acoustic wave (SAW) filter between LNA and mixer in order to make the mixer linearity requirements relaxed by attenuating the out of bands blockers [6]. Recently, some calibration circuits have been proposed to address IIP2 problem. However, they are complex and large power consuming [7], [8]. Using analog techniques and optimizing the mixer for IIP2 is another approach [9], [10].

Many predistortion and feedforward techniques have been employed for third-order distortion cancellation [11]–[13].

The derivative superposition (DS) method which is a special case of the feedforward technique uses two FETs working in different bias conditions. The third-order derivatives of the two FETs are in opposite phase of each other for the third-order distortion cancellation [14], [15]. However, due to the second-order harmonic generated in intrinsic/applied series or shunt feedback structures, the amount of improvement in the IIP3 is limited, while increasing the noise figure (NF) due to the extra components in the cancellation path. In [16], a proper phase shifting cannot be easily set by this technique in high-frequency LO signals. The linearization in resistive source degeneration technique is achieved at the cost of higher noise and higher current and power [17].

Contrary to the above techniques for separate IIP2 and IIP3 improvements, simultaneously improvement of these two still remains a challenging task.

In this paper, a new scheme cancelling simultaneously the second- and third-order distortions is introduced. The cancellation mechanism is performed in the transconductor stage of the mixer. In order to cancel the second-order intermodulation component, a signal with the same IM_2 amplitude and opposite phase is generated in an auxiliary path and fed to the output of the main path in transconductance stage, and to suppress the third-order intermodulation IM_3, low-frequency second-order intermodulation IM_2 is generated and injected to circuit to generate the IM_3 component with the same amplitude and the opposite phase.

To evaluate the proposed linearization technique, a Gilbert-cell mixer based on the proposed method has been designed and simulated. Because of superior linearity, the proposed mixer is very suitable for the applications requiring high linearity transmitters. To examine the performance of the circuit, a highly accurate nonlinear analysis based on Volterra series has been proposed too. Simulations, using practical device models, in ADS have shown good conformance between simulation and analytical results. Having good analytical equations shortens the design process.

The rest of the paper is organized as follows: Section II reviews mixer linearity analysis in CMOS downconversion mixers. In Section III, the high frequency analysis of IM_2-injection technique for IM_2 and IM_3 cancellation with Volterra

Manuscript received March 13, 2012; revised July 23, 2012 and October 02, 2012; accepted November 25, 2012. Date of publication June 03, 2013; date of current version July 24, 2013. This paper was recommended by Associate Editor A. Tasic.

M. Mollaalipour is with the Integrated Circuits Research Laboratory, Electrical and Computer Engineering Department, Babol University of Technology, 47148-71167 Babol, Mazandaran, Iran (e-mail: m.m.alipour@stu.nit.ac.ir).

H. Miar-Naimi is with the Integrated Systems Laboratory, Electrical Engineering Department, Babol University of Technology, 47148-71167 Babol, Mazandaran, Iran (e-mail: h_miare@nit.ac.ir).

Digital Object Identifier 10.1109/TCSI.2013.2239159

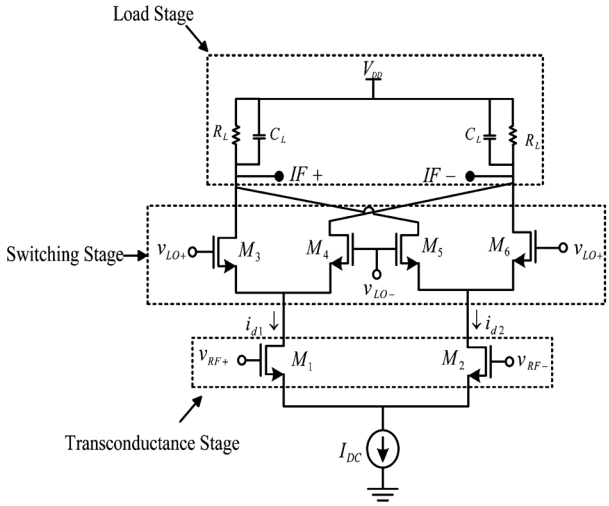

Fig. 1. Double-balanced Gilbert-type mixer.

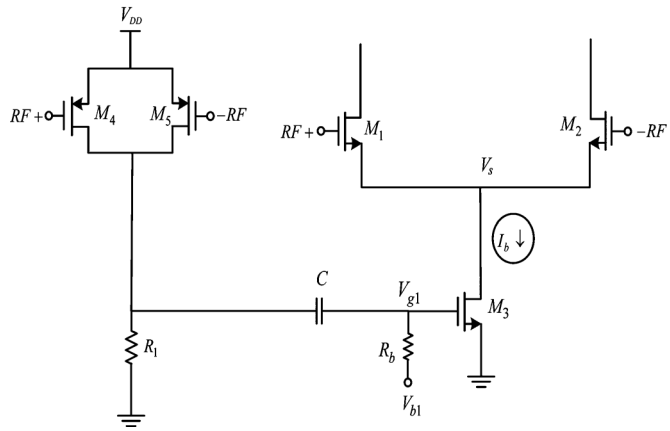

Fig. 2. Input transconductor schematic for IM_3 cancellation.

series analysis is introduced. Section IV describes the analysis of second- and third-order intermodulation distortion in switching stage with LC filter. The proposed mixer and the simulation results are given in Section V. Finally, Section VI gives the conclusions.

II. Gilbert-Cell Mixer; A Brief Introduction

Fig. 1 shows a typical Gilbert mixer. It comprises a transconductor stage, a switching stage, and a load stage.

There are several mechanisms at the origin of intermodulation in CMOS downconversion mixers: self-mixing, transconductor nonlinearity, switching pairs non-linearity, and mismatch in load resistors [18].

In Gilbert-cell mixer topology, the nonlinearity effects are mostly dominated by the input transconductor. Hence, linearization of the MOSFET transconductor stage is a significant consideration.

Considering the input-stage differential pair of the double balanced mixer, shown in Fig. 1, the Taylor series expansion of the time-varying current i_{d1} around a bias point appropriately chosen on the I-V characteristics of device M1 is expressed as:

$$i_{d1} = g_m v_{gs} + g'_m v_{gs}^2 + g''_m v_{gs}^3 + \dots . \tag{1}$$

where v_{gs} is the variation of the gate-to-source voltage around a bias point, g_m, g'_m and g''_m are the fundamental transconductance and the second/third-order nonlinearity coefficients respectively.

The second- and third-order terms in (1) are the main degrading contributions of the second- and third-order intermodulations in RF systems. Obviously the goal of every linearization technique is minimizing g'_m, g''_m for the circuit. We minimize these two coefficients by injecting a regenerated IM_2 in two different paths respectively which are explained as follows.

III. Linearization Technique With IM_2 Injection

A. IM_3 Cancellation Analysis

The IM_2 injection technique externally generates and injects a low-frequency IM_2 component into the circuit. The injected IM2 is mixed with the fundamental input signal to generate an IM3 signal required for cancellation of the intrinsic IM3 signal in the main path [19].

Fig. 2 shows the transconductor stage along with the IM_2 regenerating and injecting circuit.

The RF circuit performance is usually studied using two tone analyses, so we consider the input as below

$$v_{RF} = V_{RF}\cos(\omega_1 t) + V_{RF}\cos(\omega_2 t).$$

M1 and M2 are the input transistors of the mixer. M4, M5, and R_1 compose a squaring circuit to generate a low-frequency IM_2 current at $(\omega_1 - \omega_2)$, which is then injected through M3 into the common source node V_s of the mixer. In the transconductor stage the injected low frequency IM_2 is multiplied by fundamental tones that results in tones at $(2\omega_1 - \omega_2)$ and $(2\omega_2 - 2\omega_1)$ to cancel the IM_3 tones arising from intrinsic third-order distortion.

Since the drains of M4 and M5 are connected together, the odd-order components of their currents (the fundamental and the IM3) do not appear in the sum of their output currents and only the even order components are present.

As mentioned above, to cancel the intrinsic third-order distortion of transconductor, we should control the amplitude of the injected current.

To investigate how the cancellation mechanism works, a theoretical analysis of the circuit based on Volterra series theory with harmonic input method is introduced. This mathematical tool can provide equations that indicate how the nonlinearities of the mixer sub-cells can interact in a way to improve overall linearity performance.

At the beginning a circuit model shown in Fig. 3 is used. In this linearized transconductor, a low-frequency signal (I_b) is injected to the common-source node of the differential pair. Parasitic capacitances are also shown in the figure (that necessitates using Volterra series analysis). C_{gs} denotes the effective gate-source capacitance of the transistors. The IM_2 injected transistor (M3) is replaced with a current source I_b, in parallel to a resistor r_d (the output resistance of transistor M3), and C_t (representing parasitic capacitances affecting source node).

In Fig. 3, transistors with energy storing elements, here capacitors, force the relation between drain current of M1 and gate voltage to be a nonlinear differential equation that can be described by means of a Volterra series expansion as below.

$$I_1 = A_1(\omega) \circ V_g + A_2(\omega_1, \omega_2) \circ V_g^2 + A_3(\omega_1, \omega_2, \omega_3) \circ V_g^3. \tag{2}$$

In the equation above, A_1, A_2 and A_3 are the first-, second-, and third-order transconductance of the input transconductor,

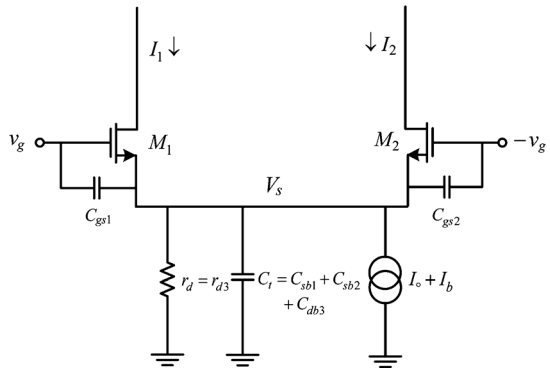

Fig. 3. Equivalent model of Input transconductor for high frequency linearity analysis.

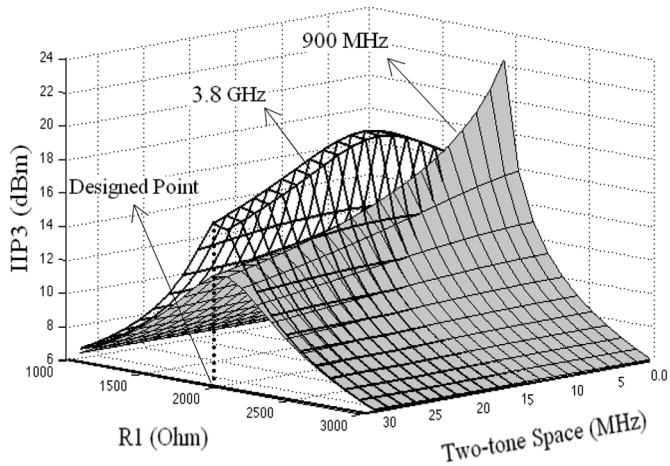

Fig. 4. Behavior of IIP3 computed with Volterra series versus frequency space between two tones and resistor R1 with different working frequency.

respectively. These three are also named the first-, second-, and third-order Volterra kernels.

A rather lengthy calculation, reported in Appendix A, leads to the expressions for these Volterra kernels shown at the bottom of the page, where $C_{t0} \approx C_{db3} + C_{sb1} + C_{sb2} + C_{gs1} + C_{gs2}$.

Equation (3) shows that first-order transconductance of the transconductor stage $(A_1(\omega))$ is equal to main transconductance of a simple transistor characteristic (g_m). Equation (4) consists of two terms where the first one stands for the IM_2 raised by the intrinsic nonlinearity of the transconductor stage, and the second term stands for IM_2 caused by the IM_2 generator (notice to the g'_{m4} in the second term). Regarding to the positive sign of the second term, we can say that IM_2 generator increases the IM_2 of the transconductor stage.

In (5) the first bracket raised from the transconductor and the second term is induced by the IM_2 generator. Regarding the opposite sign of this two terms, we can say that the IM_2 generator decreases the IM_3 of the transconductor.

From (3) and (5) the input-referred voltage intercept point for the third-order intermodulation of transconductor can be expressed as below [20].

$$IIV3 = \sqrt{\frac{4}{3}\frac{g_{m1}}{|A_3(\omega_1, \omega_2, \omega_3)|}}. \tag{6}$$

Equation (6) states that IIV3 can be infinite (for low frequency applications) if the following holds:

$$4r_d g'_{m1}\left(g_{m3} g'_{m4} R_1 - g'_{m1}\right) + g''_{m1}(1 + 2r_d g_{m1}) = 0. \tag{7}$$

In deriving the above equation, we considered (5) in which all frequencies are set to zero.

Therefore, the IIP3 of the transconductor can be improved by an appropriate choice of transistor and resistor sizes.

Fig. 4 plots the theoretical values for IIP3 as a function of the resistor R_1 and frequency space for different two-tone frequencies. The curves were plotted for 60 μm/0.18 μm aspect ratio for M1 and M2, bias current of 2 mA and 15 μm/0.18 μm aspect ratio for M4 and M5. The size of M3 is chosen to be 80 μm/0.3 μm. In the bias current, g''_{m1} has a negative value. IIP3 is calculated from (6), as the corresponding power dissipated in a 50 Ω resistor.

As shown in Fig. 4, for different working frequency and frequency spaces, the IIP3 experiences its maximum value for the same resistor (here for example $R_1 = 2\ \mathrm{k}\Omega$).

The obtained Volterra series formulas can also predict the IIP3 variation as a function of two-tone spacing and working frequency. Therefore, two RF tones varied over 900 MHz–3.2 GHz are applied to the input transconductor, whereas frequency space between them is varied within 1–30 MHz range. Fig. 5 illustrates the behavior of IIP3 of transconductor computed with Volterra series using (6) for $R_1 = 2\ \mathrm{k}\Omega$. Fig. 5 shows that cancellation performance decreases as tone spacing increases, but improves as working frequency increases.

$$A_1(\omega) = g_{m1}. \tag{3}$$

$$A_2(\pm\omega_1, \mp\omega_2) = \frac{g'_{m1}\left(1 + j(\pm\omega_1 \mp \omega_2) r_d C_{t0}\right)}{1 + 2r_d g_{m1} + j(\pm\omega_1 \mp \omega_2) r_d C_{t0}} + \frac{2g'_{m4} g_{m3} g_{m1} r_d R_1}{\left(1 + 2r_d g_{m1} + j(\pm\omega_1 \mp \omega_2) r_d C_{t0}\right)\left(1 + j(\pm\omega_1 \mp \omega_2) R_1 C_{t1}\right)}. \tag{4}$$

$$A_3(\pm\omega_1, \pm\omega_1, \mp\omega_2) = g''_{m1} - \frac{4}{3} r_d g'^2_{m1}\left(\frac{2}{1 + 2r_d g_{m1} + j(\pm\omega_1 \mp \omega_2) r_d C_{t0}} + \frac{1}{1 + 2r_d g_{m1} \pm j2\omega_1 r_d C_{t0}}\right) + \left(\frac{8/3 g_{m3} g'_{m1} g'_{m4} r_d R_1}{\left(1 + j(\pm\omega_1 \mp \omega_2) R_1 C_{t1}\right)\left(1 + 2r_d g_{m1} + j(\pm\omega_1 \mp \omega_2) r_d C_{t0}\right)} + \frac{4/3 g_{m3} g'_{m1} g'_{m4} r_d R_1}{\left(1 + j(\pm 2\omega_1) R_1 C_{t1}\right)\left(1 + 2r_d g_{m1} + j(\pm 2\omega_1) r_d C_{t0}\right)}\right). \tag{5}$$

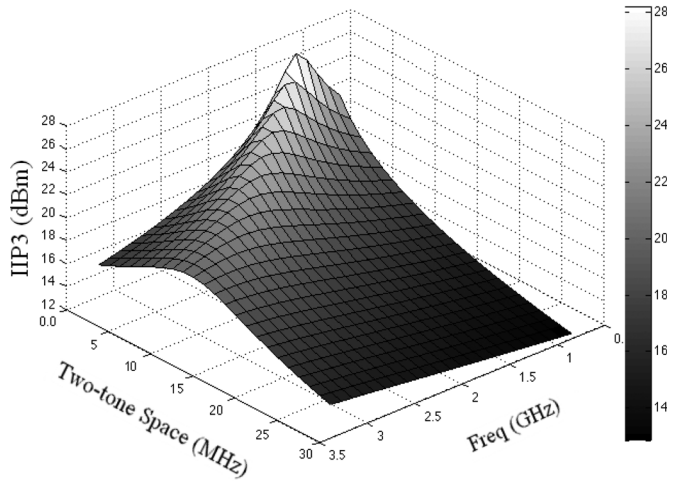

Fig. 5. Theoretical IIP3 versus frequency space between two tones and working frequency.

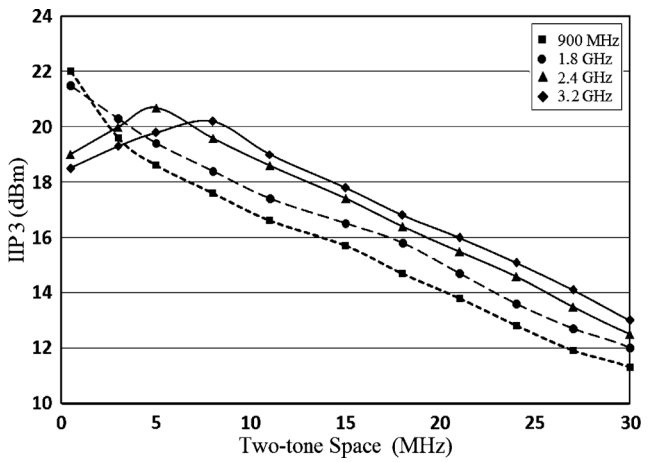

Fig. 6. Simulated IIP3 versus frequency space between two tones for different working frequency.

To validate the results of the Volterra analysis in Fig. 5, simulations in 0.18 μm RF CMOS technology using advanced design system (ADS) simulator were also carried out.

An extensive set of simulation was performed to determine how the IIP3 of the transconductor changes as a function of both frequency space between two tones and the working frequency. The simulation results are shown in Fig. 6. A good agreement with Fig. 5 is evident. As one can infer from both figures, as frequency increases, the maximum value of IIP3 is seen in higher frequency space.

Fig. 7 shows simulated and theoretical value of IIP3 for the input transconductor versus two-tone spacing, both for the proposed transconductor and the basic differential pair without any injection mechanism (without M4, M5, and R_1 from the Fig. 2 that leads to $g'_{m4} = 0$ in the second bracket of the (5)). The theoretical value of IIP3 for the basic differential pair is obtained from (5) ignoring second bracket. Two RF tones at 1.8 GHz are applied to the input transconductor, whereas frequency space between them is varied within 1–30 MHz range. This figure shows that an increase in frequency space causes a decrease in IIP3.

A very good agreement with theoretical results is observed and the good performance of the proposed transconductor is evident.

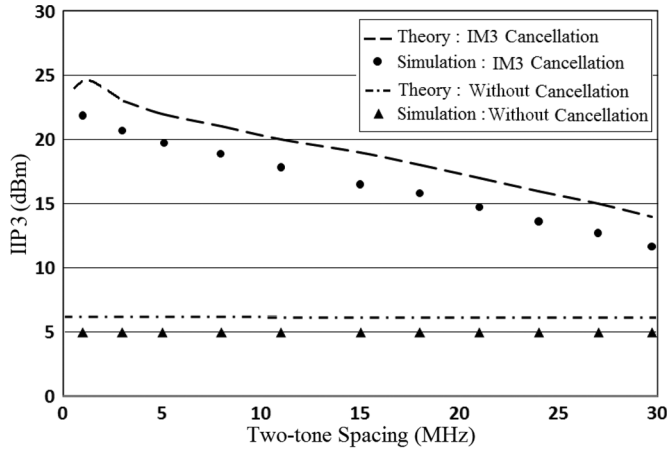

Fig. 7. IIP3 variation versus frequency space between two tones for the basic differential pair and the proposed transconductor.

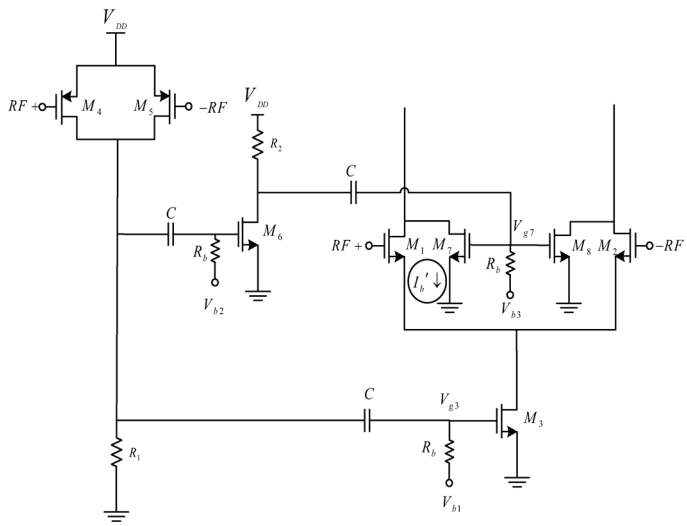

Fig. 8. Input transconductor schematic for IM_2 cancellation.

B. IM_2 Cancellation Mechanism

Implementation of the proposed IM_2 cancellation technique is shown in Fig. 8.

A signal with the same IM_2 amplitude and opposite phase is generated in an auxiliary path (M7) and is fed to the output of the main path of transconductor stage in order to cancel second-order intermodulation component. The amplitude of the injected current should be controlled to cancel the IM_2 current of transconductor.

The injected low-frequency second-order distortion current, as shown in Fig. 8, is found as below:

$$I'_b = g_{m7} V_{g7} = \underbrace{-g_{m7} \frac{2g'_{m4} g_{m6} R_1 R_2}{(1+j(\pm\omega_1 \mp \omega_2)R_1 C_{t1})\,(1+j(\pm\omega_1 \mp \omega_2)R_2 C_{t2})}}_{A'_2} V_g^2. \tag{8}$$

where $C_{t2} \approx C_{db6} + C_{gs7} + C_{gs8}$.

By means of A_2, the total second-order transfer function of transconductance can be written as $A_{2t}(A_{2t} = A_2 + A'_2)$ which results in (9), at the bottom of the next page.

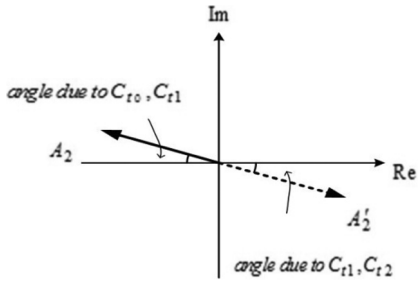

Fig. 9. Vector diagram for the IM_2 components.

Minimizing the magnitude of the second-order Volterra kernel would naturally improve the linearity performance of the transconductor, focusing on IM_2. Fig. 9 shows the vector diagram to illustrate the interaction between the different component of $A_{2t}(A_{2t} = A_2 + A_2')$.

Both real and imaginary parts of A_2 and A_2' have opposite signs. Thus A_{2t} has a magnitude less than A_2 and A_2' that means the overall IIP2 has been improved.

With a simple investigation, one can find out that the opposite directions A_2 and A_2' hold for all frequency space, $(\omega_1 - \omega_2)$. Therefore, it is expected that the improvement on IIP2 holds for all frequency offset.

From (9), the input-referred voltage intercept point for the second-order intermodulation can be expressed as follows

$$IIV2 = \frac{g_{m1}}{|A_2(\omega, \omega)|}. \tag{10}$$

Equation (10) states that low frequency IIV2 can be infinite if the following holds:

$$g'_{m1} + 2g_{m1}g_{m3}g'_{m4}r_dR_1 - 2 \cdot (1 + 2r_dg_{m1}) \cdot g'_{m4}g_{m6}g_{m7}R_1R_2 = 0. \tag{11}$$

Clearly, an appropriate choice of the parameters will lead to a large linearity improvement.

Fig. 10 shows the theoretical values for IIP2 as functions of the resistor R_2 and frequency space, with 10 μm/0.18 μm aspect ratio for M6, and 5 μm/0.18 μm for M7 and M8 biased by 150 μA. The differential IIP2 is calculated using (10) as the corresponding power dissipated in a 50 Ω resistor and assuming 0.1% mismatch between load resistors of transconductor. As shown in Fig. 4, for all frequency spaces, the IIP3 experiences its maximum for the same resistor (here for example $R_2 = 100\,\Omega$).

To have a good insight on variations of A_2 and A_2' over different frequency spaces, their real and imaginary parts have been plotted in Fig. 11 for $R_2 = 100\,\Omega$. As Fig. 11 shows, using a proper biasing for M6 and M7 the real and imaginary part of A_2 and A_2' have the same magnitude and opposite phase for all frequency spaces. This verifies the discussion above.

To evaluate the proposed IM_2 cancellation mechanisms, three different simulations have been performed as shown in Fig. 12. In the first simulation, the IIP2 of the basic transconductor without any additional cancellation circuit has been evaluated for different frequency spaces. In the second simulation, the IM_3 cancellation circuit has been added and in the third simulation, both IM_2 and IM_3 cancellation were added. For the latter case the analytical results has been plotted too.

Both theoretical and simulated IIP2 do not show strong dependency on two tone space.

Also, this figure shows that the injected frequency components at $(\omega_1 - \omega_2)$, in IM_3 cancellation mechanism, increases the total IM_2 component, which leads to a smaller IIP2.

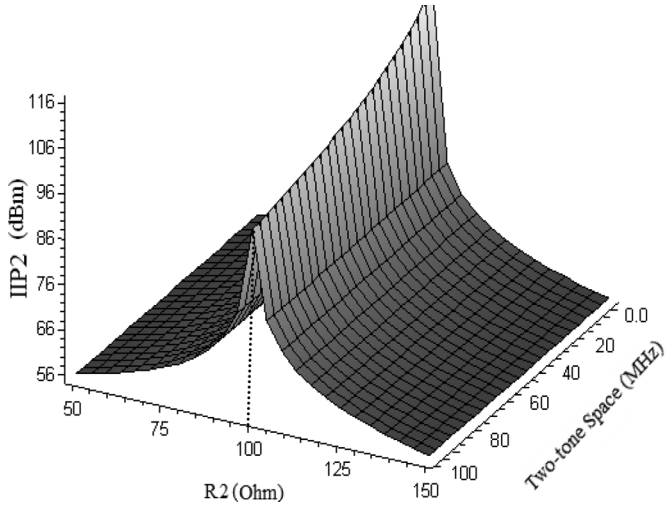

Fig. 10. Behavior of IIP2 computed with Volterra series versus resistor R2 and frequency space between two tones.

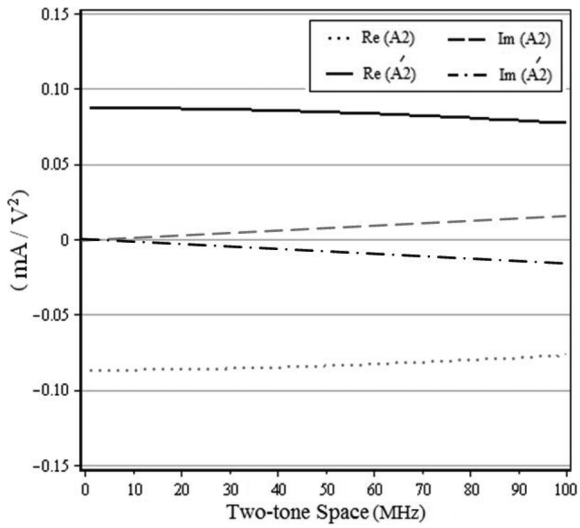

Fig. 11. Real and imaginary part of A_2 and A_2'.

$$A_{2t}(\pm\omega_1, \mp\omega_2) = \frac{g'_{m1}\,(1 + j(\pm\omega_1 \mp \omega_2)r_dC_{t0})}{1 + 2r_dg_{m1} + j(\pm\omega_1 \mp \omega_2)r_dC_{t0}} + \frac{2g'_{m4}g_{m3}g_{m1}r_dR_1}{(1 + 2r_dg_{m1} + j(\pm\omega_1 \mp \omega_2)r_dC_{t0})\,(1 + j(\pm\omega_1 \mp \omega_2)R_1C_{t1})} - \frac{2g'_{m4}g_{m6}g_{m7}R_1R_2}{(1 + j(\pm\omega_1 \mp \omega_2)R_1C_{t1})\,(1 + j(\pm\omega_1 \mp \omega_2)R_2C_{t2})}. \tag{9}$$

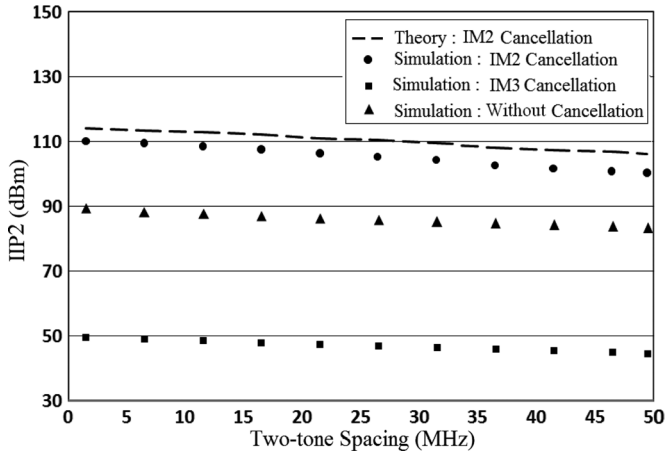

Fig. 12. Comparison between IIP2 of transconductor with and without cancellation versus frequency space between two tones.

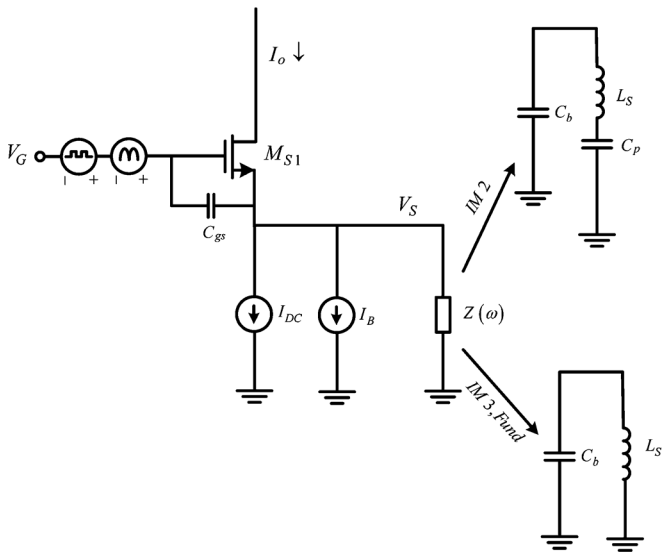

Fig. 13. Switching stage equivalent model for the analysis of second- and third-order intermodulation distortion at high frequencies.

IV. Analysis of Switching Pair Nonlinearity

Switching stage is another stage that affects on the overall IIP2 and IIP3. The nonlinearities imposed by this stage is analyzed as follows.

The parasitic capacitance loading the switching-stage at the source plays a key role in the second-order intermodulation mechanisms and is tuned out by means of an integrated inductor [18]. Also, as we investigated, the parasitic capacitance induces third-order nonlinearity too.

To analyze IM_2 and IM_3 generation mechanism, an equivalent source follower model of the switching pair shown in Fig. 13 is used. This figure shows the circuit implementation applied to a single switching pair. The overall gate voltage is given by the superposition of the rectified LO with the peak amplitude of V_{pk} plus the periodic square-wave offset, toggling between 0 and V_{off}.

The second-order distortion can be generated by the switching pair nonlinearities and also mismatches between parameters of the switching transistors [18].

The total analysis of differential output low-frequency second-order distortion with LC filter, is reported in Appendix B (B.18). By using LC filter which tunes the parasitic capacitor of switching transistors in local oscillator (LO) frequency, the IM_2 component generated by the switching pairs are minimized [9]. Also, inductor suppresses any differential low-frequency IM_2 component coming from the transconductor.

The following equation shows that using the LC filter attenuates the IM_3 resulted from the switching pair nonlinearity, and increases the fundamental tone at the output.

The third-order distortion can be generated by the switching pair nonlinearities and also mismatches between parameters of the switching transistors, where mismatch is very less significant in IM_3 generation and is ignored in our analysis.

The total differential output low-frequency third-order distortion is reported in Appendix B.

Considering the distortion that resulted from the third-order nonlinear transfer function $(G_3(\omega,\omega,\omega))$ generated by the switching pair nonlinearities, the differential output low-frequency third-order distortion current can be written as

$$\begin{aligned} I_{IM3} = &-\frac{3}{2\pi} I_{RF}^3 \cdot \left(C_s(2\omega_1-\omega_2) - \frac{1}{L_s(2\omega_1-\omega_2)} \right) \\ &\cdot \left(|G_3(\omega_1,\omega_1,-\omega_2)| \right. \\ &\cdot \cos\left((-\omega_{LO}+2\omega_1-\omega_2)t \right. \\ &\left. \left. +\angle G_3(\omega_1,\omega_1,-\omega_2)\right)\right). \end{aligned} \tag{12}$$

Current sources are considered by a two-tone RF signal as below

$$i_{RF} = I_{RF}\cos(\omega_1 t) + I_{RF}\cos(\omega_2 t).$$

Also the detailed circuit solution leading to fundamental output current is reported in Appendix B.

$$\begin{aligned} I_{FUND} = &-\left(\frac{2}{\pi} \cdot I_{RF} \left(C_s\omega_1 - \frac{1}{L_s\omega_1} \right) \right. \\ &\cdot \left(\mathrm{Re}\left(G_1(\omega_1)\right) \cdot \cos\left((-\omega_{LO}+\omega_1)\,t\right) \right. \\ &\left. \left. -\mathrm{Im}\left(G_1(\omega_1)\right) \cdot \sin\left((-\omega_{LO}+\omega_1)t\right)\right)\right) \\ &-4I_{RF}\frac{V_{Pk}}{\pi^2} \sum_{k\in z/\{0\}} \\ &\times \left(\frac{\left(C_s(2k\omega_{LO}+\omega_1) - \frac{1}{L_s(2k\omega_{LO}+\omega_1)}\right)}{(1-4k^2)(2k+1)} \right. \\ &\cdot \left(\mathrm{Re}\left(F_{11}(\omega_1, 2k\omega_{LO})\right) \cdot \cos\left((-\omega_{LO}+\omega_1)t\right) \right. \\ &-\mathrm{Im}\left(F_{11}(\omega_1, 2k\omega_{LO})\right) \\ &\left. \left. \cdot \sin\left((-\omega_{LO}+\omega_1)t\right)\right)\right) \\ &-\frac{2}{\pi} I_{RF}\sin(-\omega_{LO}+\omega_1)t. \end{aligned} \tag{13}$$

The effectiveness of using LC filter is demonstrated in Figs. 14 and 15, which represent simulated fundamental and third-order distortion products down-converted from first LO harmonic as a function of inductor L_s together with theoretical values.

The $100\ \mu\mathrm{m}/0.18\ \mu\mathrm{m}$ switching pair is biased at 2 mA, with 0.6 pF source capacitance for 5-dBm LO power. A 9.5 nH inductor L_s is chosen to resonate out the parasitic capacitor at the local oscillator frequency at 2.1 GHz.

At the resonance frequency of the filter all the fundamental current directly flow to the output while other distortion frequencies generated by switching stage especially IM_2 and IM_3 are bypassed by the filter and have no way to the output.

The IM_3 generated by the transconductor directly flows to the output, because the IM_3 frequency is very close to the fundamental frequency. This leads to a small increase on the

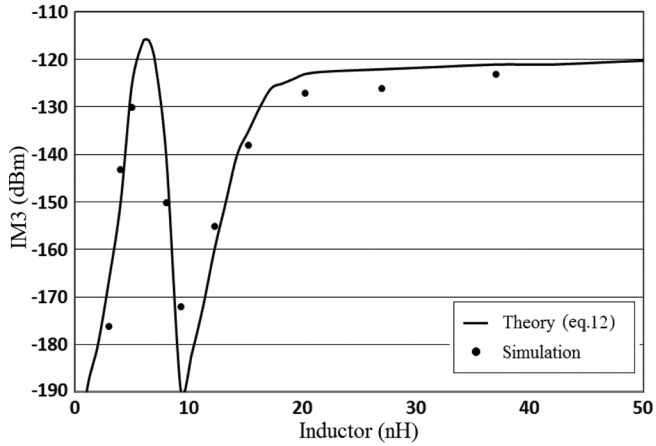

Fig. 14. Theoretical (solid line) and simulated (dots) output IM_3 due to switching pair intermodulation distortion with LC filter.

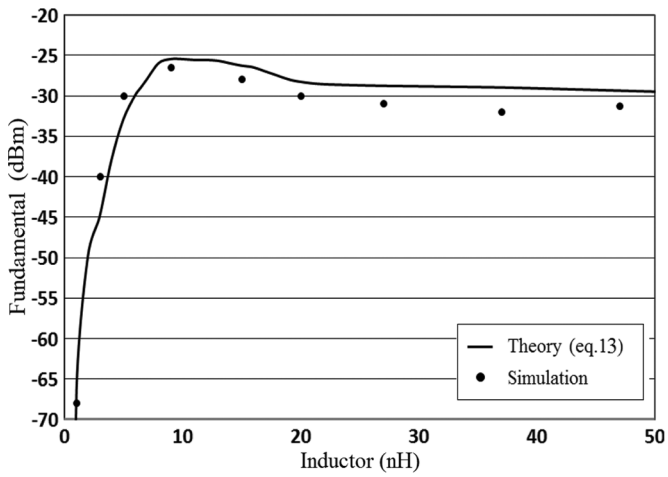

Fig. 15. Theoretical (solid line) and simulated (dots) output fundamental power in switching pair output with LC filter.

IM_3 caused by transconductor. As shown later on Fig. 17(a) the overall IIP3 is improved overall.

V. Simulation Results

The fully differential down conversion mixer, shown in Fig. 16, has been simulated using 0.18 μm CMOS TSMC model by Advanced Design System (ADS) software. The biasing current is set to 4 mA, as a compromise between noise and linearity in the switching stage.

The M1 and M2 transistors with the size of 70 $\mu\mathrm{m}/0.18\ \mu\mathrm{m}$ are biased by 1.85 mA. The switching transistors are driven by a local oscillator with 6 dBm power and the size of $100\ \mu\mathrm{m}/0.18\ \mu\mathrm{m}$. The size of M7 and M8 transistors is chosen $5\ \mu\mathrm{m}/0.18\ \mu\mathrm{m}$ which is lower than the size of M1 and M2 transistors in order to achieve less noise and capacitive load and are biased by 150 μA.

M4 and M5 are designed to be $10\ \mu\mathrm{m}/0.18\ \mu\mathrm{m}$, and the IM_2 amplitude can be designed properly by choosing appropriate dc bias of M4 and M5, as it was mentioned. The random mismatch between switching transistors is modeled by 2 mV offset voltage. Also the LO frequency is 2.1 GHz.

In order to assess the linearity improvement due to the second harmonic injection technique, the second- and third-order input intercept points (IIP2, IIP3) of the proposed mixer with and without the LC filter and its comparison with conventional Gilbert-type mixer are presented in Fig. 17. Simultaneous cancellation of the second- and third-order distortions leads

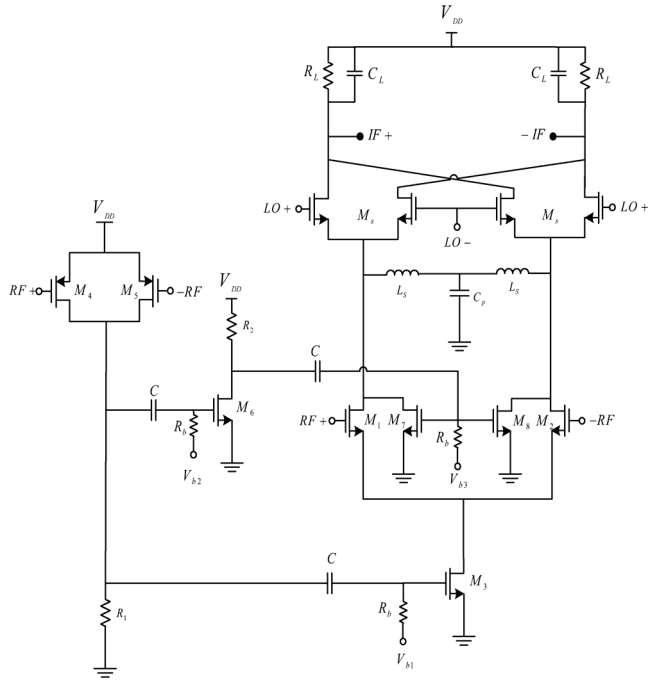

Fig. 16. Circuit schematic of the proposed Gilbert-cell mixer.

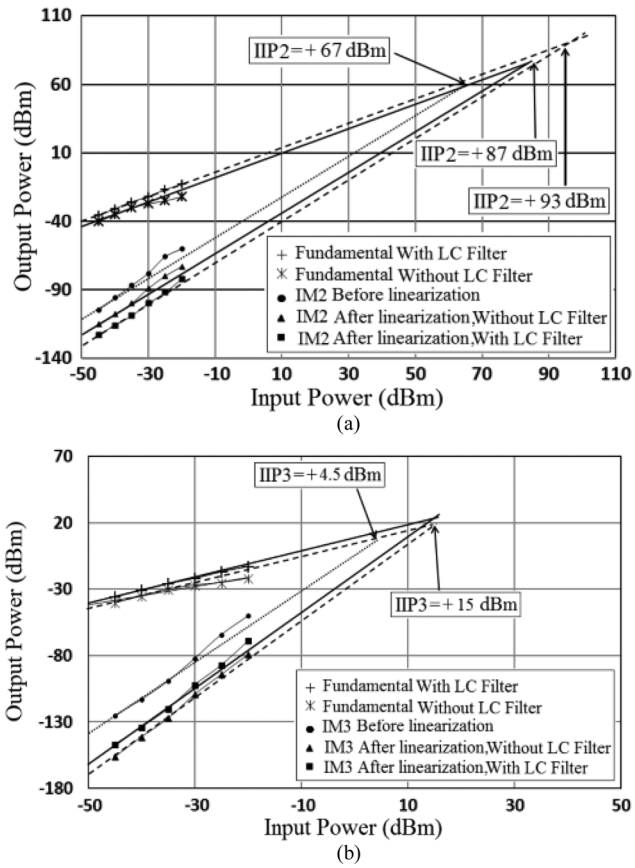

Fig. 17. Simulated (a) IIP2 and (b) IIP3 of the proposed mixer with and without LC filter, and its comparison with conventional Gilbert-type mixer with equal power consumptions.

to an extraordinary IIP3 improvement of +10 dB and IIP2 improvement of +26 dB.

The switching stage transistors and nonlinear capacitance at the common-source node are considered as the main sources of flicker noise in Gilbert-cell mixers.

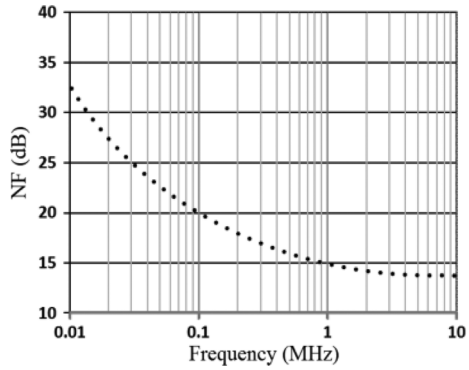

Fig. 18. Noise performance of the mixer.

TABLE I
SIMULATION PERFORMANCE SUMMARY AND COMPARISON WITH PRIOR PUBLISHED WORKS

REF	This Work	[7]	[9]	[15]	[21]
Process	0.18μm	65nm	0.18μm	0.18μm	0.18μm
Frequency(GHz)	2.1	2.1	2.1	2.4	2.4
IIP2 (dBm)	+93	+90	+82	N/A	N/A
IIP3 (dBm)	+15	+6	+10	+15	+ 9
Power (mW)	8	6	7.2	14.8	5.4
Gain (dB)	15	12	16	11	16.5
NF (dB)	14	17.5	18.5	13.8	14.2

The input referred noise, which is in-band averaged noise (10 kHz–1.9 MHz), is less than 3.7 nV/sqrt(Hz). The mixer NF performance is shown in Fig. 18.

Table I summarizes the simulation results of the most important performance parameters of the proposed mixer and compares them with designs reported in the literature. Clearly, this cancellation technique provides an extraordinary linearity.

VI. CONCLUSION

A low IM_2 and IM_3 distortion mixer exploiting the second- and third-order distortion cancellation is presented and analyzed using Volterra series. Simulations using TSMC 0.18 μm CMOS model technology exhibits 10 dB and 26 dB improvements in IIP3 and IIP2. In this method, the excess power consumption is low and the NF doesn't increase significantly. The proposed cancellation technique can be applied to many wireless communication systems which require highly linear RF front-ends and noise performance.

APPENDIX A
DERIVATION OF THE VOLTERRA OPERATORS FOR THE TRANSCONDUCTOR STAGE

In this section derivation of the Volterra series kernels for intermodulation components in the output current of the circuit shown in Fig. 3 is presented.

By considering (1), I_1 and I_2 are expressed as:

$$\begin{aligned} I_1 &= g_{m1}(V_g - V_s) + g'_{m1}(V_g - V_s)^2 + g''_{m1}(V_g - V_s)^3 + \dots \\ I_2 &= g_{m1}(-V_g - V_s) + g'_{m1}(-V_g - V_s)^2 \\ &\quad + g''_{m1}(-V_g - V_s)^3 + \dots \end{aligned} \tag{A.1}$$

The symbols g_m, g'_{m1} and g''_{m1} denote the first-, second-, and third-order transconductances of the transistor M1.

The source voltage is related to the applied input signal by the following Volterra series expansion [22]–[24]:

$$\begin{aligned} V_s =& N_1(\omega) \circ I_b + M_1(\omega) \circ V_g + M_1(\omega) \circ (-V_g) \\ &+ M_2(\omega,\omega) \circ V_g^2 + M_2(\omega,\omega) \circ (-V_g)^2 \\ &+ M_3(\omega,\omega,\omega) \circ V_g^3 + M_3(\omega,\omega,\omega) \circ (-V_g)^3 \\ &+ K_{11}(\omega,\omega) \circ I_b \circ V_g + K_{11}(\omega,\omega) \circ I_b \circ (-V_g). \end{aligned} \tag{A.2.a}$$

$$V_s = N_1(\omega) \circ I_b + 2M_2(\omega,\omega) \circ V_g^2 + \dots \tag{A.2.b}$$

By applying the Kirchhoff law at V_s node we get:

$$\begin{aligned} I_1 + I_2 &= I_b + (C_{db3} + C_{sb1} + C_{sb2})\frac{dV_s}{dt} \\ &\quad + C_{gs1}\frac{d(V_s - V_g)}{dt} + C_{gs2}\frac{d(V_s + V_g)}{dt} + \frac{V_s}{r_d} \\ I_1 + I_2 &= I_b + C_{t1}\frac{dV_s}{dt} + \frac{V_s}{r_d} \end{aligned} \tag{A.3}$$

where $C_{t0} \approx C_{db3} + C_{sb1} + C_{sb2} + C_{gs1} + C_{gs2}$.

Considering (A.1) and (A.3), the Volterra kernel in (A.2) is calculated as

$$N_1(\omega) = -\frac{r_d}{1 + 2r_d g_{m1} + j\omega r_d C_{t0}}. \tag{A.4.a}$$

$$M_2(\pm\omega_1, \mp\omega_2) = \frac{r_d g'_{m1}}{1 + j(\pm\omega_1 \mp \omega_2) r_d C_{t0} + 2r_d g_{m1}}. \tag{A.4.b}$$

Substituting (A.4) into (A.2) and comparing the resulted expression with (2), we can write

$$\begin{aligned} I_1 = &-(g_{m1}N_1)I_b + (g_{m1})V_g - (2g'_{m1}N_1)\,V_g I_b \\ &+ (g'_{m1} - 2g_{m1}M_2)\,V_g^2 + (g''_{m1} - 4g'_{m1}M_2)\,V_g^3. \end{aligned} \tag{A.5}$$

Also the current I_b of transistor M3 can be expressed versus V_g as below

$$I_b = g_{m3}V_{g1} = g_{m3}\frac{2g'_{m4}R_1}{(1 + j(\pm\omega_1 \mp \omega_2)R_1 C_{t1})}V_g^2. \tag{A.6}$$

where $C_{t1} \approx C_{db4} + C_{db5} + C_{gs3} + C_{gs6}$.

From (A.5), (A.6), and (2), $A_1(\omega)$, $A_2(\omega,\omega)$, and $A_3(\omega,\omega,\omega)$ can be concluded. (See equations at the bottom of the next page.)

APPENDIX B
EXPANDED VOLTERRA SERIES ANALYSIS OF SWITCHING STAGE

Referring to the circuit in Fig. 13, we look for the second- and third-order intermodulation components in the output current by nonlinearity in the switching stage.

The voltage applied to the gate of the input stage transistor consists of a square wave, toggling between 0 and V_{off} with period T_{LO} and a large rectified sinusoid.

By using (1), the solution is found by applying the Kirchhoff law at the source node, and expressing V_S versus the applied input signals by means of a Volterra series expansion [21]–[23].

$$\begin{aligned} V_s =& H_1(\omega) \circ V_G + \dots \\ &+ F_{11}(\omega,\omega) \circ V_G \circ I_B + F_{12}(\omega,\omega,\omega) \circ V_G \circ I_B^2 + \dots \\ &+ G_1(\omega) \circ I_B + G_2(\omega,\omega) \circ I_B^2 \\ &+ G_3(\omega,\omega,\omega) \circ I_B^3 + \dots \end{aligned} \tag{B.1}$$

where other Volterra kernels have been omitted as they play less significant or no role at all in the following analysis.

Below, the Volterra kernels used in the analysis of the mixer switching pair are derived. V_G and V_S denote the gate and source voltages while g_m, g_2 and g_3 are the intrinsic transconductance of the switching transistor. $Y(\omega)$ is an admittance loading the common source node of the switching pair.

$$H_1(\omega) = \frac{j\omega C_{gs} + g_m}{Y(\omega)}. \tag{B.2.a}$$

$$F_{11}(\omega_1, k\omega_{LO}) = \frac{2g_2\left(Y(k\omega_{LO}) - (g_m + jk\omega_{LO}C_{gs})\right)}{Y(\omega_1 + k\omega_{LO}) \cdot Y(k\omega_{LO}) \cdot Y(\omega_1)}. \tag{B.2.b}$$

$$F_{12}(k\omega_{LO}, \omega_1, \omega_2) = \frac{Y(k\omega_{LO}) - (g_m + jk\omega_{LO}C_{gs})}{Y(k\omega_{LO} \pm \omega_1 \mp \omega_2) \cdot Y(k\omega_{LO}) \cdot Y(\pm\omega_1) \cdot Y(\mp\omega_2)} \cdot \left(-2g_2^2\left(\frac{1}{Y(k\omega_{LO} \pm \omega_1)} + \frac{1}{Y(k\omega_{LO} \mp \omega_2)} + \frac{1}{Y(\pm\omega_1 \mp \omega_2)}\right) + 3g_3\right). \tag{B.2.c}$$

$$G_1(\omega) = \frac{-1}{Y(\omega)}. \tag{B.2.d}$$

$$G_2(\pm\omega_1, \mp\omega_2) = \frac{g_2}{Y(\pm\omega_1 \mp \omega_2) \cdot Y(\pm\omega_1) \cdot Y(\mp\omega_2)}. \tag{B.2.e}$$

$$G_3(\pm\omega_1, \pm\omega_1, \mp\omega_2) = \frac{-1}{Y^2(\pm\omega_1) \cdot Y(\mp\omega_2) \cdot Y(\pm 2\omega_1 \mp \omega_2)} \cdot \left[\frac{2}{3}g_2^2\left(\frac{1}{Y(\pm 2\omega_1)} + \frac{2}{Y(\pm\omega_1 \mp \omega_2)}\right) - g_3\right]. \tag{B.2.f}$$

Firstly, consider the effect of the switching stage nonlinearity on generating IM_3 at the output.

Using $G_3(\omega, \omega, \omega)$ (third-order input current cube to source voltage transfer function of switching stage), the sidebands in the source voltage spectrum are found as below

$$V_s = G_3(\omega, \omega, \omega) \cdot i_{RF}^3. \tag{B.3}$$

The corresponding sidebands current spectrum in the impedance Z is given by

$$I_Z = C_s\frac{dV_s}{dt} + \frac{1}{L_s}\int V_s \cdot dt \tag{B.4}$$

where $C_s \approx C_{gs} + C_b$. From (B.3) and (B.4), assuming $i_{RF} = I_{RF}(\cos(\omega_1 t) + \cos(\omega_2 t))$, the following expression for I_Z is obtained.

$$I_{Z1} = \frac{3}{8}I_{RF}^3 \cdot Y(2\omega_1 - \omega_2) \cdot \left(G_3(\omega_1, \omega_1, -\omega_2)e^{j(2\omega_1 - \omega_2)t} - G_3(-\omega_1, -\omega_1, \omega_2) \cdot e^{-j(2\omega_1 - \omega_2)t}\right). \tag{B.5}$$

The differential output low-frequency third-order distortion current is calculated as a low-pass filtered product of the current I_Z times a square-wave function toggling between 1 and -1 with a duty cycle equal to 50%.

The Fourier series expansion of the square-wave can be expressed as

$$P = \frac{2}{j\pi}\sum_{k\in\mathrm{Z}}\frac{e^{j(2k+)\omega_{LO}t}}{(2k+1)}. \tag{B.6}$$

The obtained output intermodulation current is given by:

$$\begin{aligned} i_{out,3rd1} &= I_{Z1} \cdot P \\ &= -\frac{3}{2\pi}I_{RF}^3 \cdot \left(C_s(2\omega_1 - \omega_2) - \frac{1}{L_s(2\omega_1 - \omega_2)}\right) \\ &\quad \cdot (\mathrm{Re}\left(G_3(\omega_1, \omega_1, -\omega_2)\right)\cos\left((-\omega_{LO} + 2\omega_1 - \omega_2)\,t\right) \\ &\quad - \mathrm{Im}\left(G_3(\omega_1, \omega_1, -\omega_2)\right) \\ &\quad \times \sin\left((-\omega_{LO} + 2\omega_1 - \omega_2)\,t\right)). \end{aligned} \tag{B.7}$$

$$A_1(\omega) = g_{m1}. \tag{A.7.a}$$

$$A_2(\pm\omega_1, \mp\omega_2) = \frac{g'_{m1}\left(1 + j(\pm\omega_1 \mp \omega_2)r_d C_{t0}\right)}{1 + 2r_d g_{m1} + j(\pm\omega_1 \mp \omega_2)r_d C_{t0}} + \frac{2g'_{m4}g_{m3}g_{m1}r_d R_1}{\left(1 + 2r_d g_{m1} + j(\pm\omega_1 \mp \omega_2)r_d C_{t0}\right)\left(1 + j(\pm\omega_1 \mp \omega_2)R_1 C_{t1}\right)}. \tag{A.7.b}$$

$$A_3(\pm\omega_1, \pm\omega_1, \mp\omega_2) = \frac{4}{3}g_{m3}g'_{m1}g'_{m4}r_d R_1 \cdot \left(\frac{2}{\left(1 + j(\pm\omega_1 \mp \omega_2)R_1 C_{t1}\right)\left(1 + 2r_d g_{m1} + j(\pm\omega_1 \mp \omega_2)r_d C_{t0}\right)} + \frac{1}{\left(1 + j(\pm 2\omega_1)R_1 C_{t1}\right)\left(1 + 2r_d g_{m1} + j(\pm 2\omega_1)r_d C_{t0}\right)}\right) - \frac{4}{3}r_d g'^2_{m1}\left(\frac{2}{1 + 2r_d g_{m1} + j(\pm\omega_1 \mp \omega_2)r_d C_{t0}} + \frac{1}{1 + 2r_d g_{m1} \pm j2\omega_1 r_d C_{t0}}\right) + g''_{m1} \tag{A.7.c}$$

Secondly, consider the effect of the transconductor stage nonlinearity on generating IM_3 at the output.

Distortion of the current flowing through the impedance Z is found by means of $G_1(\omega)$ and $F_{11}(\omega,\omega)$.

Using $G_1(\omega)$, (first-order input current to source voltage transfer function) the sidebands current spectrum in the impedance Z is given as follows:

$$V_s = G_1(\omega)\cdot i_{3rd}. \tag{B.8}$$

$$\begin{aligned} I_{Z2} =& \frac{1}{2}\cdot I_{3RD}\cdot Y(2\omega_1-\omega_2) \\ &\times\Big(G_1(2\omega_1-\omega_2)e^{j(2\omega_1-\omega_2)t} \\ &\quad -G_1(-2\omega_1+\omega_2)\cdot e^{-j(2\omega_1-\omega_2)t}\Big). \end{aligned} \tag{B.9}$$

where

$$i_{3rd} = \underbrace{I_{3RD}}_{I_{RF}^3}(\cos(2\omega_1-\omega_2)t)$$

Again the sideband current is downconverted at baseband by a square wave toggling between 1 and -1 with 50%-duty cycle. The resulting output intermodulation current is given as below

$$\begin{aligned} i_{out,3rd2} =& I_{Z2}\cdot P \\ =& \left(-\frac{4}{\pi}\cdot I_{3RD}\cdot\left(C_s(2\omega_1-\omega_2)-\frac{1}{L_s(2\omega_1-\omega_2)}\right)\right. \\ &\times(\mathrm{Re}(G_1(2\omega_1-\omega_2))\cos((-\omega_{LO}+2\omega_1-\omega_2)t) \\ &\quad -\mathrm{Im}(G_1(2\omega_1-\omega_2)) \\ &\quad \left.\times\sin((-\omega_{LO}+2\omega_1-\omega_2)t))\right). \end{aligned} \tag{B.10}$$

$F_{11}(\omega,\omega)$, the second-order nonlinear transfer function with linear input voltage and input current, is only responsible for sidebands around $2k\omega_{LO}$, $(2k+1)\omega_{LO}$.

The sidebands around odd harmonics of the LO frequency due to the offset voltage at the gate, are ignored because they are small.

For sidebands around even LO harmonics of the LO frequency due to the equivalent rectified sinusoid at the gate, the distortion current is given by

$$V_s = F_{11}(\omega,\omega)\cdot I_b\cdot V_G. \tag{B.11}$$

$$V_G = \frac{2V_{Pk}}{\pi}\sum_{k\in z/\{0\}}\frac{e^{j2k\omega_{LO}t}}{1-4k^2}. \tag{B.12}$$

$$\begin{aligned} I_{Z3} =& \frac{1}{2}I_{3RD}\frac{2V_{Pk}}{\pi}\sum_{k\in z/\{0\}}\frac{e^{j2k\omega_{LO}t}}{1-4k^2}\cdot \\ &\cdot Y(2k\omega_{LO}+(2\omega_1-\omega_2)) \\ &\times\Big(F_{11}(\omega,2k\omega_{LO})e^{j(2\omega_1-\omega_2)t} \\ &\quad -F_{11}(-\omega,-2k\omega_{LO})\cdot e^{-j(2\omega_1-\omega_2)t}\Big). \end{aligned} \tag{B.13}$$

V_G is Fourier series expansion of the rectified sinusoid at gate.

The current is downconverted at baseband by the switching stage with a square wave.

The resulting output intermodulation current is calculated as shown at the bottom of the page.

Finally, the effect of direct leakage on generating IM_3 at the output is considered as below

$$\begin{aligned} i_{out,3rd4} =& i_{in,3rd}\cdot P \\ =& -\frac{2}{\pi}I_{3RD}(\sin(2\omega_1-\omega_2-\omega_{LO})). \end{aligned} \tag{B.15}$$

The total differential output low-frequency third-order distortion current can be written as shown in the equation at the top of the next page. By considering total output third-order distortion current, the total differential output fundamental current is found as shown similarly.

$$\begin{aligned} I_{FUND} =& -\left(\frac{2}{\pi}\cdot I_{RF}\left(C_s\omega_1-\frac{1}{L_s\omega_1}\right)\right. \\ &\cdot(\mathrm{Re}(G_1(\omega_1))\cdot\cos((-\omega_{LO}+\omega_1)t) \\ &\quad \left.-\mathrm{Im}(G_1(\omega_1))\cdot\sin((-\omega_{LO}+\omega_1)t))\right) \\ &-4I_{RF}\frac{V_{Pk}}{\pi^2} \\ &\times\sum_{k\in z/\{0\}}\left(\frac{\left(C_s(2k\omega_{LO}+\omega_1)-\frac{1}{L_s(2k\omega_{LO}+\omega_1)}\right)}{(1-4k^2)(2k+1)}\right. \\ &\quad\times(\mathrm{Re}(F_{11}(\omega_1,2k\omega_{LO})) \\ &\quad\cdot\cos((-\omega_{LO}+\omega_1)t) \\ &\quad-\mathrm{Im}(F_{11}(\omega_1,2k\omega_{LO})) \\ &\quad\left.\cdot\sin((-\omega_{LO}+\omega_1)t))\right) \\ &-\frac{2}{\pi}I_{RF}(\sin(-\omega_{LO}+\omega_1)t). \end{aligned} \tag{B.17}$$

$$\begin{aligned} i_{out,3rd3} =& I_{Z3}\cdot P \\ =& -4I_{3RD}\frac{V_{Pk}}{\pi^2}\sum_{k\in z/\{0\}} \\ &\times\left(\frac{\left(C_s(2k\omega_{LO}+(2\omega_1-\omega_2))-\frac{1}{L_s(2k\omega_{LO}+(2\omega_1-\omega_2))}\right)}{(1-4k^2)(2k+1)}\right. \\ &\quad\times(\mathrm{Re}(F_{11}((2\omega_1-\omega_2),2k\omega_{LO}))\cos((-\omega_{LO}+(2\omega_1-\omega_2))t)-\mathrm{Im}(F_{11}((2\omega_1-\omega_2),2k\omega_{LO})) \\ &\quad\left.\times\sin((-\omega_{LO}+(2\omega_1-\omega_2))t))\right). \end{aligned} \tag{B.14}$$

$$
\begin{aligned}
I_{IM3} = & -\left(C_s(2\omega_1-\omega_2)-\frac{1}{L_s(2\omega_1-\omega_2)}\right)\\
& \cdot\left(\left(\frac{3}{2\pi}I_{RF}^3\cdot\mathrm{Re}\left(G_3(\omega_1,\omega_1,-\omega_2)\right)+\frac{2}{\pi}\cdot I_{3RD}\cdot\mathrm{Re}\left(G_1(2\omega_1-\omega_2)\right)\right)\cdot\cos\left(\left(-\omega_{LO}+2\omega_1-\omega_2\right)t\right)\right.\\
& \left.-\left(\frac{3}{2\pi}I_{RF}^3\cdot\mathrm{Im}\left(G_3(\omega_1,\omega_1,-\omega_2)\right)+\frac{2}{\pi}\cdot I_{3RD}\cdot\mathrm{Im}\left(G_1(2\omega_1-\omega_2)\right)\right)\cdot\sin\left(\left(-\omega_{LO}+2\omega_1-\omega_2\right)t\right)\right)\\
& -4I_{3RD}\frac{V_{Pk}}{\pi^2}\sum_{k\in z/\{0\}}\left(\frac{\left(C_s\left(2k\omega_{LO}+(2\omega_1-\omega_2)\right)-\frac{1}{L_s(2k\omega_{LO}+(2\omega_1-\omega_2))}\right)}{(1-4k^2)(2k+1)}\right.\\
& \qquad\times\left(\mathrm{Re}\left(F_{11}\left((2\omega_1-\omega_2),2k\omega_{LO}\right)\right)\cos\left(\left(-\omega_{LO}+(2\omega_1-\omega_2)\right)t\right)\right.\\
& \qquad\left.\left.-\mathrm{Im}\left(F_{11}\left((2\omega_1-\omega_2),2k\omega_{LO}\right)\right)\sin\left(\left(-\omega_{LO}+(2\omega_1-\omega_2)\right)t\right)\right)\right)\\
& -\frac{2}{\pi}I_{3RD}\left(\sin\left(\left(-\omega_{LO}+(2\omega_1-\omega_2)\right)t\right)\right). \qquad \text{(B.16)}
\end{aligned}
$$

$$
\begin{aligned}
I_{IM2,odd} = & \,2\frac{V_{off}}{\pi^2}I_{RF}^2\\
& \cdot\sum_{k\in N}\left[\frac{\left(C_s(2k+1)\omega_{LO}+\frac{1}{\frac{1}{C_p(2k+1)\omega_{LO}}-L_s(2k+1)\omega_{LO}}\right)}{(2k+1)^2}\right.\\
& \qquad\cdot\left(-2A_2\mathrm{Im}\left(F_{11}\left((2k+1)\omega_{LO},(\pm\omega_1\mp\omega_2)\right)\right)\right.\\
& \qquad\left.\left.+A_1^2\mathrm{Im}\left(F_{12}\left((2k+1)\omega_{LO},\pm\omega_1,\mp\omega_2\right)\right)\right)\right]\cdot\cos(\Delta\omega t) \qquad \text{(B.18.a)}
\end{aligned}
$$

$$
\begin{aligned}
I_{IM2,even} = & +4\frac{V_{off}}{\pi^2}I_{RF}^2\\
& \cdot\sum_{k\in N/\{0\}}\left[\frac{\left(C_s(2k)\omega_{LO}+\frac{1}{\frac{1}{C_p(2k)\omega_{LO}}-L_s(2k)\omega_{LO}}\right)}{(1-4k^2)}\right.\\
& \qquad\cdot\left(2A_2\mathrm{Im}\left(F_{11}\left(2k\omega_{LO},(\pm\omega_1\mp\omega_2)\right)\right)\right.\\
& \qquad\left.\left.+A_1^2\mathrm{Im}\left(F_{12}\left((2k)\omega_{LO},\pm\omega_1,\mp\omega_2\right)\right)\right)\right]\cdot\left(\cos(\Delta\omega t)\right) \qquad \text{(B.18.b)}
\end{aligned}
$$

As briefly discussed in [18], distortion demodulated from around odd and even harmonics as well as considering a direct leakage of distortion generated by the second-order transfer function $F_{11}(\omega,\omega)$, the total second-order intermodulation components at downconversion mixer output with LC filter can be written as shown in (B.18.a)–(B.18.b) at the top of the page. Equation (B.18.a)–(B.18.b) shows that second-order distortion generated by the switching pair is directly proportional to the offset voltage V_{off}. Moreover, the second-order distortion depends on the impedance loading at the common source node through F_{11} and F_{12}, as well as on the LO frequency.

REFERENCES

[1] M. Terrovitis and R. G. Meyer, "Intermodulation distortion in current-commutating CMOS mixers," *IEEE J. Solid-State Circuits*, vol. 35, no. 10, pp. 1461–1473, Oct. 2000.

[2] I. Elahi, K. Muhammad, and P. T. Balsara, "IIP2 and DC offsets in the presence of leakage at LO frequency," *IEEE Trans. Circuits Syst. II, Exp. Briefs*, vol. 53, no. 8, pp. 647–651, Aug. 2006.

[3] B. Gilbert, "A precise four quadrant multiplier with sub nanosecond response," *IEEE J. Solid-State Circuits*, vol. SC-3, no. 12, pp. 365–373, Dec. 1968.

[4] P. J. Sullivan, B. A. Xavier, and W. H. Ku, "Low voltage performance of a microwave CMOS Gilbert cell mixer," *IEEE J. Solid-State Circuits*, vol. 32, no. 7, pp. 1151–1155, Jul. 1997.

[5] A. A. Abidi, "General relations between IP2, IP3, and offsets in differential circuits and the effects of feedback," *IEEE Microw. Wireless Compon. Lett.*, vol. 51, no. 5, pp. 1610–1612, Jun. 2003.
[6] J. Rogin, I. Kouchev, G. Bre nna, D. Tschopp, and Q. Huang, "A 1.5-V 45-mW direct-conversion WCDMA receiver IC in 0.13-m CMOS," *IEEE J. Solid-State Circuits*, vol. 38, no. 12, pp. 2239–2248, Dec. 2003.
[7] M. B. Vahidfar and O. Shoaei, "A high IIP2 mixer enhanced by a new calibration technique for zero-If receivers," *IEEE Trans. Circuits Syst. II, Exp. Briefs*, vol. 55, no. 3, pp. 219–223, Mar. 2008.
[8] Dufrene, Z. Boos, and R. Weigel, "Digital adaptive IIP2 calibration scheme for CMOS downconversion mixers," *IEEE J. Solid-State Circuits*, vol. 43, no. 11, pp. 2434–2445, Nov. 2008.
[9] M. Brandolini, P. Rossi, D. Sanzogni, and F. Svelto, "A +78 dBm IIP2 CMOS direct downconversion mixer for fully integrated UMTS receivers," *IEEE J. Solid-State Circuits*, vol. 41, no. 3, pp. 552–559, Mar. 2006.
[10] M. Brandolini, M. Sosio, and F. Svelto, "A 750 mV fully integrated direct conversion receiver front-end for GSM in 90 nm CMOS," *IEEE J. Solid-State Circuits*, vol. 42, no. 6, pp. 1310–1317, Jun. 2007.
[11] T. J. Ellis, "A modified feed-forward technique for mixer linearization," in *Proc. IEEE MTT-S Int. Microwave Symp.*, Jun. 1998, vol. 3, pp. 1423–1426.
[12] Y. Kim, Y. Kim, and S. Lee, "Linearized mixer using predistortion technique," *IEEE Microw. Wireless Compon. Lett.*, vol. 12, no. 6, pp. 204–205, Jun. 2002.
[13] S. Ayazian and R. Gharpurey, "Feedforward interference cancellation in radio receiver front-ends," *IEEE Trans. Circuits Syst. II, Exp. Briefs*, vol. 54, no. 10, pp. 902–906, Oct. 2007.
[14] T. Wook Kim, B. Kim, and K. Lee, "Highly linear receiver front-end adopting MOSFET transconductance linearization by multiple gated transis-tors," *IEEE J. Solid-State Circuits*, vol. 39, no. 1, pp. 223–229, Jan. 2004.
[15] K.-H. Liang, C.-H. Lin, H.-Y. Chang, and Y.-J. Chan, "A new linearization technique for CMOS RF mixer using third-order transconduc tance cancellation," *IEEE Microw. Wireless Compon. Lett.*, vol. 18, no. 5, pp. 350–352, Jan. 2008.
[16] S. Otaka, M. Ashida, M. Ishii, and T. Itakura, "A 10-dBm SiGe mixer with cancellation technique," *IEEE J. Solid-State Circuits*, vol. 39, no. 12, pp. 2333–2341, Dec. 2004.
[17] K. Kuo and A. Leuciuc, "A linear MOS transconductor using source degeneration and adaptive biasing," *IEEE Trans. Circuits Syst. II, Analog. Digit. Signal Process.*, vol. 48, no. 10, pp. 937–943, Oct. 2001.
[18] D. Manstretta, M. Brandolini, and F. Svelto, "Second-order inter-modulation mechanisms in CMOS downconverters," *IEEE J. Solid-State Circuits*, vol. 38, no. 3, pp. 394–406, Mar. 2003.
[19] S. Lou and H. C. Luong, "A linearization technique for RF receiver front-end using second-order-intermodulation injection," *IEEE J. Solid-State Circuits*, vol. 43, no. 11, pp. 2404–2412, Nov. 2008.
[20] B. Razavi, *RF Microelectronics*. Upper Saddle River, NJ, USA: Prentice-Hall PTR, 1998.
[21] S. Lou and H. C. Luong, "Highly linear receiver front-end adopting MOSFET transconductance linearization by multiple gated transistors," *IEEE J. Solid-State Circuits*, vol. 39, no. 1, pp. 223–229, Jan. 2004.
[22] S. Boyd, L. O. Chua, and C. A. Desoer, "Analytical Foundations of Volterra Series," *IMA J. Math. Control Inf.*, vol. 1, pp. 243–282, May 1984.
[23] C. Corduneanu and I. Sandberg, *Volterra Equations and Applications*, 1st ed. Amsterdam, The Netherlands: OPA, Jan. 2000.
[24] S. J. Gifford, "Volterra series analysis of nonlinear structures," Ph.D. dissertation, Univ. Heriot-Watt, Edinburgh, U.K., 1989.

Marzieh Mollaalipour received the B.Sc. degree in electrical engineering in 2009 and M.Sc. degree in 2012 from Mazandaran University, Faculty of Technology and Engineering, Babol, Iran.

She is a Member of the Integrated Circuit Research Laboratory, Babol University of Technology, Iran. Her main research interests include CMOS RF circuits for wireless communications, nonlinear circuit theory and applications with particular focus on down-conversion mixers.

Hossein Miar-Naimi received the B.Sc. degree from Sharif University of Technology, Iran, in 1994, the M.Sc. degree from Tarbiat Modares University, Iran, in 1996, and the Ph.D. degree from Iran University of Science and Technology in 2002.

Since 2003 he has been a Member of the Electrical and Computer Engineering Faculty of Babol University of Technology, Iran, where he later held the position of Associate Professor of Microelectronic Engineering. Since 2006 he is acting as a chairman of the Electrical and Computer Engineering Faculty. His research interests are analog CMOS integrated circuit design, nonlinear circuit theory and applications, RF microelectronics, image processing, and Evolutional algorithm.